

# Off-axis reference beam for full-field swept-source OCT and holoscopy

Dierck Hillmann,<sup>1,\*</sup> Hendrik Spahr,<sup>3</sup> Helge Sudkamp,<sup>3</sup>  
 Carola Hain,<sup>3</sup> Laura Hinkel,<sup>1</sup> Gesa Franke,<sup>3</sup>  
 Gereon Hüttmann<sup>2,3,4</sup>

March 14, 2017

<sup>1</sup>Thorlabs GmbH, Maria-Goeppert-Str. 5, 23562 Lübeck, Germany

<sup>2</sup>Medizinisches Laserzentrum Lübeck GmbH, Peter-Monnik-Weg 4, 23562 Lübeck, Germany

<sup>3</sup>Institut für Biomedizinische Optik, Universität zu Lübeck, Peter-Monnik-Weg 4, 23562 Lübeck, Germany

<sup>4</sup>Airway Research Center North (ARCN), Member of the German Center for Lung Research (DZL), Germany

\* [dhillmann@thorlabs.com](mailto:dhillmann@thorlabs.com)

In numerous applications, Fourier-domain optical coherence tomography (FD-OCT) suffers from a limited imaging depth due to signal roll-off, a limited focal range, and autocorrelation noise. Here, we propose a parallel full-field FD-OCT imaging method that uses a swept laser source and an area camera in combination with an off-axis reference, which is incident on the camera at a small angle. As in digital off-axis holography, this angle separates autocorrelation signals and the complex conjugated mirror image from the actual signal in Fourier space. We demonstrate that by reconstructing the signal term only, this approach enables full-range imaging, i.e., it increases the imaging depth by a factor of two, and removes autocorrelation artifacts. The previously demonstrated techniques of inverse scattering and holoscopy can then numerically extend the focal range without loss of lateral resolution or imaging sensitivity. The resulting, significantly enhanced measurement depth is demonstrated by imaging a porcine eye over its entire depth, including cornea, lens, and retina. Finally, the feasibility of *in vivo* measurements is demonstrated by imaging the living human retina.

## 1 Introduction

Fourier-domain optical coherence tomography (FD-OCT) is nowadays widely used to image the human eye. It can acquire three-dimensional tomograms of its anterior and posterior segment at an imaging speed and resolution not attainable with other methods. However, standard confocal FD-OCT relies on mechanical lateral scanning, which limits the obtainable imaging speed. Even more importantly, when increasing the acquisition rate, image quality suffers as the number of photons collected per A-scan decreases [1].

Therefore, lateral parallelization of the OCT data acquisition can enhance imaging speed in two ways: First, it removes the lateral scanning and thus the mechanical movement. Second, it illuminates all spots simultaneously, and thus alleviates the limits implied by the maximum permissible exposure and allows higher irradiance on the sample and thus higher data acquisition rates without harming patients – particularly for retinal imaging. The highest possible parallelization uses an area camera as detector and a tunable light source to acquire the spectrally resolved backscattered light [2]. The acquisition speed of this full-field swept-source OCT (FF-SS-OCT) is finally limited by the frame rate of the camera. With frame rates of 100,000 fps, retina imaging at 1.5 million A-scan per second was successfully demonstrated [3]. With even further increased imaging speed and due to its resulting phase stability, new applications of full-field OCT emerged recently. In particular, it was possible to image pulse-induced pressure wave in the human retina [4] and to computationally correct imaging aberrations and image photo receptor cells *in vivo* [5] and even visualize their function [6].

Generally, imaging depth in FD-OCT is restricted by the spectral resolution of the interference of sample and reference radiation. In swept-source OCT, this is determined by the instantaneous coherence length of the swept-source, and huge measurement depths have been demonstrated using scanning OCT with large coherence length lasers (see e.g. [7]). On the other hand, imaging depth in FF-SS-OCT is still limited by the instantaneous coherence length of the light source since no long-coherence lasers are available at the required sweep rates.

An alternative to long coherence length lasers is the use of full-range techniques. FD-OCT is only capable to detect absolute optical path length differences between sample and reference but not their sign. Ultimately this ambiguity results from the impossibility to detect the spectral phase and obtain the complex spectrum, and it reduces the measurement depth by a factor 2. Various full-range techniques can resolve this complex conjugate ambiguity in FD-OCT, doubling the measurement depth. In contrast to this, in classical and digital holography this complex conjugate ambiguity results in a twin image being overlaid with the object information and is in most cases solved by using off-axis reference illumination (see e.g. [8–11]). Similarly, an off-axis reference beam in FD-OCT can also resolve this ambiguity and was successfully applied to FF-SS-OCT for full-range imaging [12] and later to line-field OCT [13].

Even when high spectral resolution (high coherence length lasers) or full-range techniques provide large imaging depth in FD-OCT, an additional problem arises as the Rayleigh range should be equally large to cover this measurement depth. Outside this focal range the images are defocussed and reduced sensitivity due to confocal gating. Especially at high NA, where good lateral resolution is anticipated, this becomes increasingly challenging; in particular, the imaging depth is not sufficient to image both cornea and lens or even the retina, and axial scanning needs to be employed (see e.g. [14]). For full-field swept-source OCT, techniques of inverse scattering [15, 16] and holoscopy [17–20] were shown theoretically and experimentally, respectively. These techniques increase the focal depth by numerically compensating the defocus.

Here we demonstrate that in addition to doubling the effective imaging depth, using the off-axis reference removes major coherent artifacts of FF-SS-OCT and holoscopy, which are caused by self-interference of the sample radiation. The improvement of image quality by suppressing autocorrelation noise is investigated for imaging human retina. This way, the SNR improves by 6dB, and high quality retina images were obtained with 7.2 million A-scans per second. We also demonstrate that the off-axis recording geometry can be used for holoscopic imaging of an entire porcine eye, while nearly preserving both sensitivity and lateral resolution over an imaging depth of more than 25mm. Retina as well as cornea and lens were simultaneously imaged sharply.

## 2 Theory

Holography, digital holography, holoscopy, and full-field swept-source optical coherence tomography record interference images that are a superposition of a reference wave  $R(x, y, k)$  with waves  $O(x, y, k)$  scattered from a sample. Whereas in holography only a single wavelength is employed, the latter two techniques acquire the resulting spatial interference patterns  $I(x, y, k)$  for multiple wave numbers  $k$  as a function of lateral coordinates  $x$  and  $y$ . The recorded interference signal is given by

$$\begin{aligned}
 I(x, y, k) &\propto |R(x, y, k) + O(x, y, k)|^2 \\
 &= |R|^2(x, y, k) && \text{(DC)} \\
 &\quad + |O|^2(x, y, k) && \text{(autocorrelation)} \\
 &\quad + (R^*O)(x, y, k) && \text{(signal)} \\
 &\quad + (O^*R)(x, y, k). && \text{(conjugated signal)}
 \end{aligned}$$

The tomographic image information is contained in the signal term  $(R^*O)(x, y, k)$ , while the DC part, autocorrelation signal  $|O|^2(x, y, k)$ , and conjugated signal  $(O^*R)(x, y, k)$  disturb the actual imaging, as shown for FD-OCT in Fig. 1a. DC and autocorrelation part are thereby caused by self-interference of reference and object, respectively. When evaluating these data, the DC part causes a high signal at zero-delay, the autocorrelation term causes artifacts also referred to as coherence noise, and the conjugated signal term results in an image mirrored at the zero-delay plane. The conjugated signal thus results in the inability of OCT to distinguish positive time-delays from negative time-delays and effectively reduces the imaging depth by a factor of 2. To circumvent this limitation, full-range techniques are capable to extract the signal term and to double the measurement depth. However, they require additional information, as for instance provided by small additional mechanical (axial) scanning or multiple detectors (e.g. [14]). In holography, the image degradation caused by the additional terms was first avoided by Leith and Upatnieks by introducing an angle between the reference and the sample radiation [8]. In off-axis holography, this causes the diffraction angles to significantly differ for the signal term, the conjugated signal term and the autocorrelation term. The same principle is commonly applied in digital holography, where the signal term is isolated by numerical filtering after Fourier transforming the recorded interference pattern (Fig. 1c).

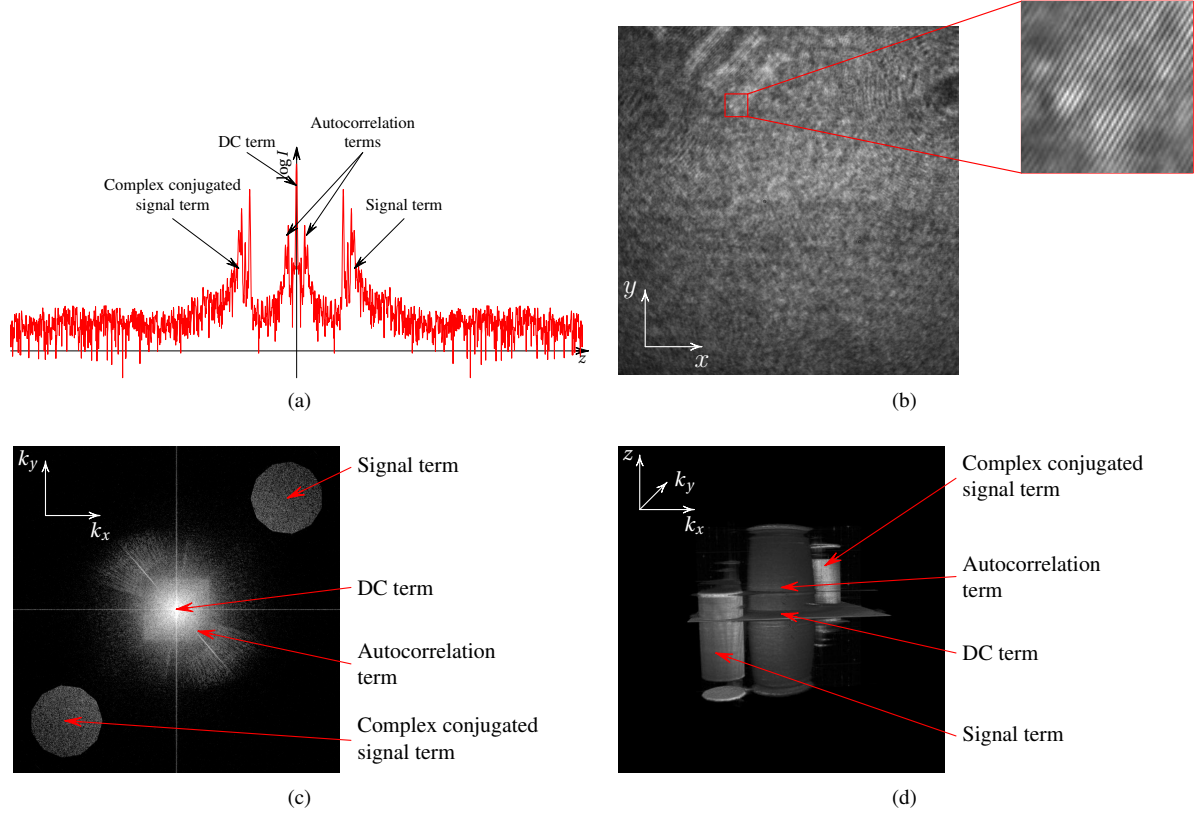


Figure 1: DC, autocorrelation, and cross-correlation (signal and conjugate signal) terms in Fourier-domain OCT. a) A-scan of an infrared viewing card. b) Fringe pattern in the intensity pattern on the camera introduced by the off-axis reference beam. c) Fourier transform of the interference pattern. The aperture is directly visible in the Fourier transform. d) Three-dimensional Fourier transform of the data cube obtained by acquiring the interference pattern of scotch tape placed in the image plane at 1024 equispaced wavenumbers, as recorded for FF-SS-OCT. The spatial frequencies are shown at their correct depth. All four terms are visible and can be separated by choosing the adequate region in Fourier space.

For a mathematical description of the resulting signals, we assume a reference wave on the camera that is traveling in arbitrary direction

$$R(x, y, k) = R_0 \exp\left(i\vec{k} \cdot \vec{x}\right) \Big|_{z=z_0},$$

where  $R_0$  is the reference wave amplitude,  $\vec{x} = (x, y, z)$  is a spatial position,  $\vec{k}$  is the wave vector, also determining the direction of the wave, and  $z_0$  specifies the camera plane, which is assumed to be parallel to the  $xy$ -plane. The wave vector  $\vec{k}$  can be decomposed into  $\vec{k}_\perp$  and  $\vec{k}_\parallel$ , the component orthogonal and parallel to the camera surface, respectively. Accordingly, the reference wave can be rewritten as

$$R(x, y, k) = R_0 \exp\left(i\vec{k}_\parallel \cdot \vec{x}\right) \exp\left(i\vec{k}_\perp \cdot \vec{x}\right) \Big|_{z=z_0}.$$

The first exponential only depends on the lateral  $x$ - and  $y$ -coordinates and the second only on  $z$  and is therefore constant in the camera plane  $z = z_0$ . Computing the Fourier transform of the reference light with respect to the  $x$ - and  $y$ -coordinates yields the zero frequency

$$\mathcal{F}_{xy} \left[ |R|^2 \right] = \mathcal{F} \left[ R_0^2 \right] = R_0^2 \delta(k_x, k_y).$$

With these results, a Fourier transform of the interference signal gives

$$\begin{aligned} \mathcal{F}_{xy} [I(x, y, k)] &= \gamma \left( R_0^2 \delta(k_x, k_y) + \mathcal{F}_{xy} \left[ |O|^2 \right] + \right. \\ &\quad \left. + \left( R_0 \delta(\vec{k} - \vec{k}_\parallel) * \mathcal{F}_{xy} [O^*] \right) + \left( R_0^* \delta(\vec{k} + \vec{k}_\parallel) * \mathcal{F}_{xy} [O] \right) \right), \end{aligned}$$





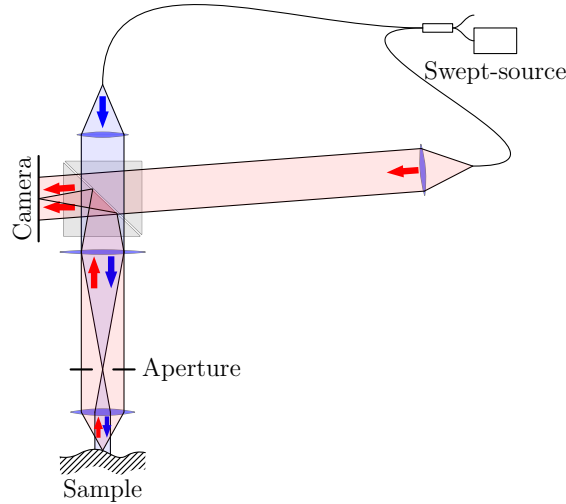


Figure 3: Mach-Zehnder type interferometer used for off-axis FF-SS-OCT and holoscopy. Light emitted by a swept laser source was split into sample and reference arm by a fiber coupler. The sample was illuminated by a collimated beam and the backscattered light was imaged onto the camera. The reference illuminated the camera under a sufficient angle to separate the image from autocorrelation noise. For *in vivo* measurements the objective lens was replaced by the lens of the eye.

both on-axis and off-axis reference illumination for variable imaging magnifications. For off-axis imaging, the angle was chosen to sufficiently discriminate the different signal terms by using a live display of the Fourier transformed camera image. Polarization of both sample and reference arm was matched to optimize contrast in the interference signal.

A Basler ace acA2040-180km CMOS camera was used for *ex vivo* measurements. Maximum frame rate was 180 frames/s at  $2048 \times 2048$  pixels resolution. The wavelength sweep of the laser was synchronized with the image acquisition to record 2048 images during one sweep.

For *in vivo* measurements, a much faster CMOS camera (Photron FASTCAM SA-Z) was used. The area of interest was reduced to  $896 \times 368$  pixels to enable an acquisition rate of about 60,000 frames/s. To further increase imaging speed, only 512 images were recorded during one wavelength sweep. *In vivo* imaging with on-axis and off-axis reference beam resulted in different image parameters (Table 1). With on-axis reference imaging, the NA was up to 0.2 and an equivalent A-Scan rate of 38.6 MHz was reached. For off-axis imaging the usable bandwidth was reduced by a factor of 2.3 in  $x$  and  $y$  direction. To completely filter the autocorrelation noise this was insufficient, however, it only reduced the effective A-scan rate by a factor of 5.4. For both on-axis and off-axis imaging, the radiant flux on the sample of 5.2 mW was limited by the output of the swept source. Total energy per A-scan was 0.14 nJ for imaging at 0.2 NA with the on-axis reference beam and 0.72 nJ with the off-axis reference beam, due to the 5.4 times reduced A-scan rate at unchanged field of view.

Table 1: Imaging parameters for on-axis and off-axis FF-SS-OCT.

	Off-axis	On-axis
Effective A-scan rate	7.2 MHz	38.6 MHz
Numerical Aperture	0.09	0.21
Max. power on sample	5.2 mW	5.2 mW
Max. power on sample per A-scan	$0.085 \mu\text{W}$	$0.016 \mu\text{W}$
Max. energy on sample per A-scan	0.72 nJ	0.14 nJ

### 3.1 Evaluation of signal-to-noise ratio for *in vivo* measurements

As a measure of image quality the signal-to-noise ratio of *in vivo* retinal images was determined. En-face slices of nearly homogeneous speckle structures and of noise in front of the retina were evaluated and for each region a histogram of the amplitude values was created. Both, the amplitude of noise in unaveraged OCT images and of homogeneous speckle structures in the signal follow the Rayleigh probability distribution, as both are described by random phasor sums [22]. Thus, this distribution was fit to the histograms of noise and signal, respectively. The expectation values of the resulting distributions were taken to compute the signal-to-noise ratio (SNR). To compare the SNR for on-axis and off-axis, the

same structures of the same retina were evaluated. For comparison, scanned OCT images of the retina were taken using a commercial spectrometer-based OCT system (Thorlabs Hyperion) with a central wavelength of 840nm and an A-scan rate of 127kHz.

## 4 Results and discussion

### 4.1 Efficient suppression of coherent noise and full-range imaging

Generally, Fourier-domain OCT images of scotch tape layers show coherent noise. In scanning OCT this autocorrelation noise is low, since the confocal gating suppresses out-of-focus light, and although scotch tape layers are visible outside the Rayleigh length, they do not act as efficient sources for interference with the other layers. On the other hand, full-field OCT images of scotch tape layers are dominated by coherent noise (Fig. 4a), if they are acquired with an on-axis reference. FF-SS-OCT and holoscopy detect reflected light from all tape layers with the same efficiency. Thus autocorrelation signals not only show up near the zero-delay line at the top of the image but in the whole reconstructed volume. The strongly reflecting layers cause autocorrelation signals significantly decreasing image quality.

Off-axis recording efficiently suppressed this coherent autocorrelation noise (Fig. 4b). When the signal term was separated by filtering in the Fourier plane a similar image quality compared to scanned OCT was obtained. The off-axis recording did not only separate the image information from the autocorrelation, but it also resolved the ambiguity with respect to positive and negative path length differences between sample and reference radiation. When the zero path length delay is within the scotch tape, all layers are clearly visible without overlap at their correct position, either below or above the zero path length (Fig. 4d). Thus off-axis recording of the interference pattern and filtering in the Fourier domain enabled full-range OCT with minimal artifacts at the zero delay.

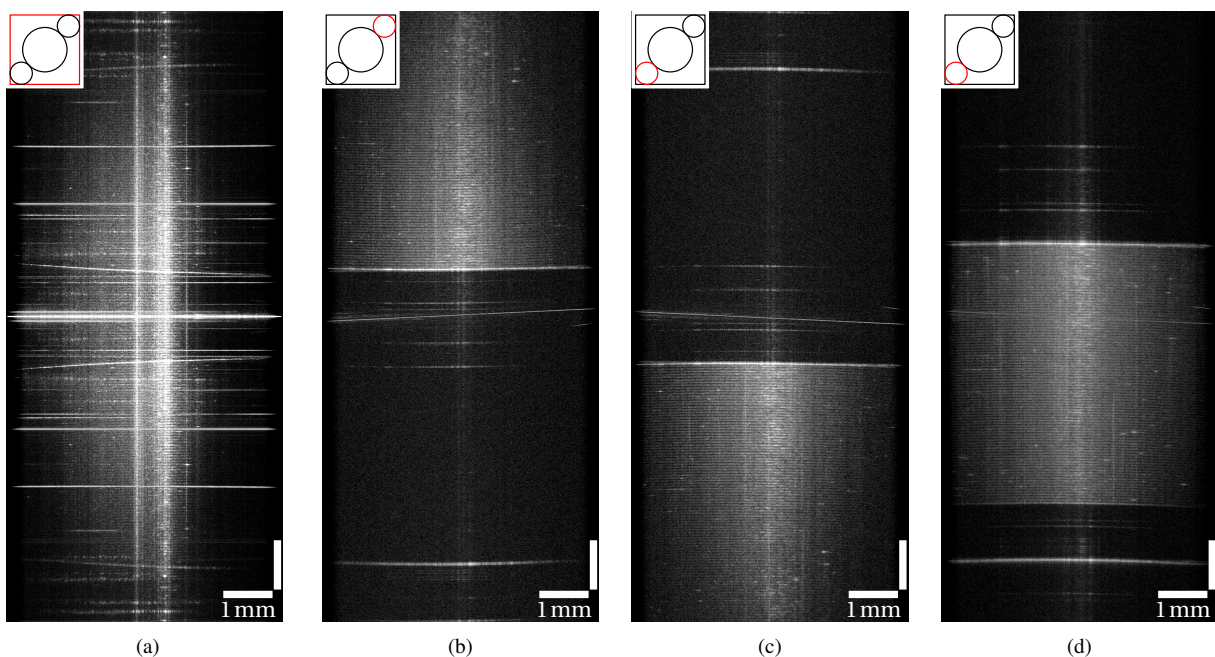


Figure 4: B-scans taken from data cubes of scotch tape recorded with full-field swept-source OCT . a) Without rejection of the autocorrelation signal major artifacts are visible. Both, the image and the conjugated image are visible. b, c) Reconstruction after removal of the DC and autocorrelation terms by filtering in the Fourier space. Coherent noise is significantly reduced. No conjugated image is visible. The full depth range above and below the zero delay can be used. d) Artifact-free full-range imaging allows to position the zero optical delay line within the scotch tape; negative and positive path length differences are resolved. Insets show schematically filtering (red line) in the Fourier plane.

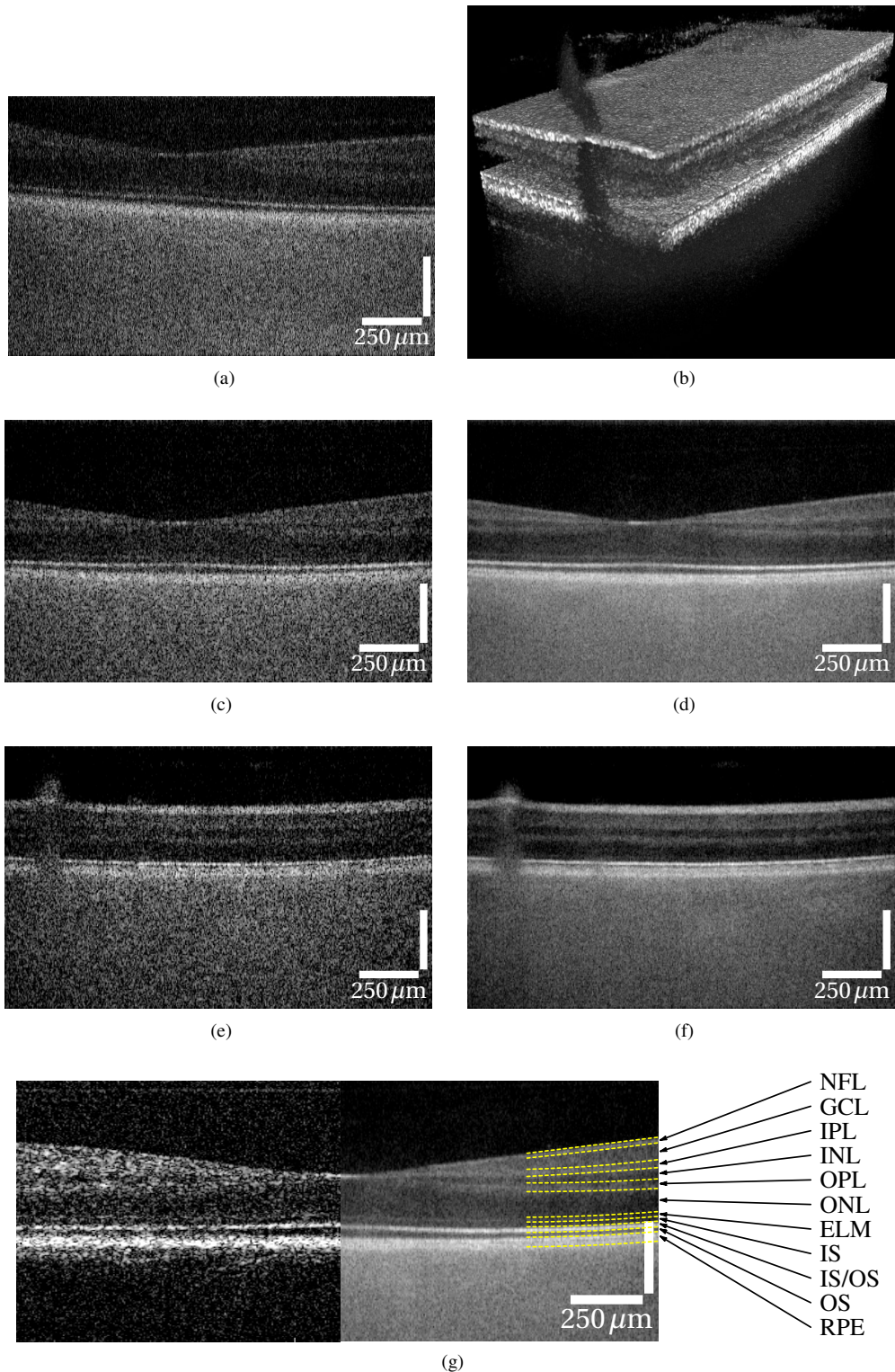


Figure 5: *In vivo* retinal images acquired with OCT. a) Macula imaged with on-axis FF-SS-OCT. b) Volume rendering of the dataset shown in f. c, d) Off-axis FF-SS-OCT images of the macula; unaveraged single slice and average of ten lateral B-scans, respectively. e, f) Off-axis FF-SS-OCT images of retinal periphery; unaveraged single slice and average of 10 lateral B-Scans, respectively. g) Macular region of human retina imaged by FF-SS-OCT in comparison to scanning OCT. Layers of the retina visible in FF-SS-OCT. NFL = nerve fiber layer, GCL = ganglioncell layer, IPL = inner plexiform layer, INL = inner nuclear layer, OPL = outer plexiform layer, ONL = outer nuclear layer, ELM= external limiting membrane, IS = photoreceptor inner segments, IS/OS = photoreceptor inner and outer segment junction, OS = photoreceptor outer segments, RPE = retinal pigment epithelium.

## 4.2 Improved SNR for *in-vivo* measurements

Using the high speed CMOS camera human retina was measured *in vivo* at 7.2 million A-scans/s with off-axis reference (Fig. 5a, c, e). To enhance the imaging quality, which was compromised by the low signal level at the high imaging speed, volumetric data sets of OCT images were cross-correlated, shifted accordingly in all three dimensions, and averaged (Fig. 5b, d, f).

Given the acquisition speed, which was significantly faster than that of commercially available OCT devices, image quality of the full-field system is remarkable. All retinal layers that are usually visible in OCT imaging can be clearly distinguished (see Fig. 5g). Intensities of the different layers above the RPE differ only slightly between FF-SS-OCT and scanned OCT. Below the RPE the choroid shows high signal intensities, but hardly any structures. Here mostly multiple scattered photons were detected due to the lack of a confocal gating. Photons from the strongly scattering RPE [23] or choroid are always assigned to depths higher than the depth of any of their scattering events and thus below the RPE. Therefore they disturb imaging of the choroid, but do not corrupt imaging of the neuronal layers.

Table 2: Signal-to-noise ratio (SNR) at the retinal pigment epithelium (RPE) for different measurement geometries and sample power image at the macula. While the SNR in on-axis geometry for  $10\times$  radiant flux on the sample increased by 1.2dB, the SNR can be significantly increased by using off-axis reference illumination and lateral filtering.

Sample power	SNR (dB)	
	On-axis	Off-axis
0.5 W	17.7	17.2
5 mW	18.9	25.2
SNR gain (dB)	1.2	8.0

Although with off-axis imaging the lateral dimension and therefore radiant flux and energy of each A-scan are increased, the overall detection aperture is decreased in order to sample the interference pattern correctly; both effects, higher flux and reduced aperture, are expected to compensate each other if scattering is isotropic. Hence, a similar SNR for on-axis and off-axis imaging is expected, if shot noise dominates coherence noise. And indeed, at 0.5 mW on the sample similar SNR values of 17.7dB and 17.2dB were observed for on-axis and off-axis imaging, respectively (see Table 2).

When using on-axis FF-SS-OCT, a tenfold increase of the radiant power on the sample from 0.5 mW to 5 mW improved SNR only by 1.2dB instead of the expected 10dB. Since the signal is proportional to the square root of the number of photo electrons  $N_O$  from the sample

$$S \propto \sqrt{N_R N_O},$$

and the noise is dominated by shot noise

$$\sigma_\gamma = \sqrt{N_R + N_O},$$

with  $N_R$  photo electrons detected from the reference arm, for  $N_R \ll N_O$  the SNR will increase with the square root of  $N_O$ .

However, the autocorrelation term, i.e., coherence noise, can become significant compared to the shot noise  $\sigma_\gamma$ , if the number of sample photons  $N_O$  increases in comparison to the number of reference photons  $N_R$ . The coherence noise  $\sigma_{AC}$  is directly proportional to the number of photo electrons from the sample, i.e.,

$$\sigma_{AC} = \alpha N_O,$$

with  $\alpha \leq 1$  being a suitable proportionality constant depending on the signal depth  $z$  and the sum of the autocorrelation noise from all depths not exceeding the number of sample photons. This yields

$$SNR \propto \frac{\sqrt{N_R N_O}}{\sqrt{N_R + N_O + \alpha^2 N_O^2}}.$$

Finally, restricting the total number of photo electrons to the full well capacity  $N$  of the detector, i.e., imposing

$$N = N_R + N_O,$$

the SNR scales with  $N_O$  as shown in Figure 6 for different values of  $\alpha$ .



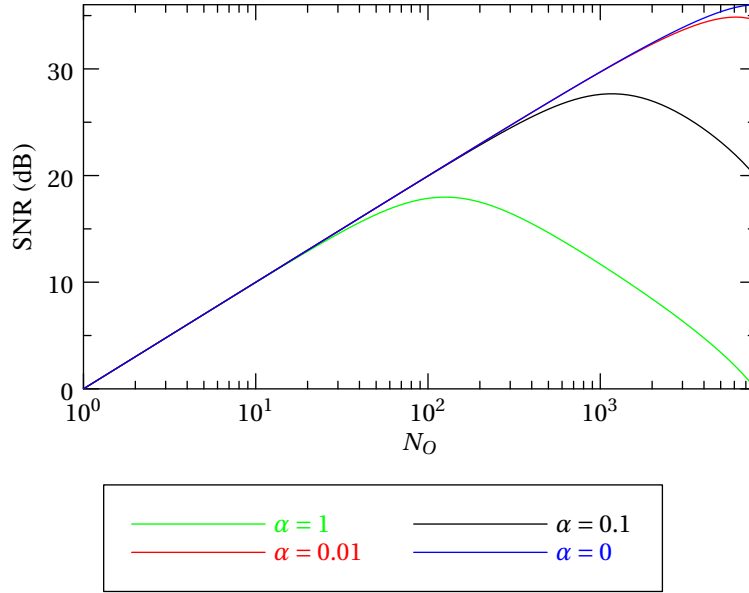


Figure 6: Signal-to-noise ratio for different  $\alpha$  for a fixed full well capacity of  $N = 16000$  electrons. A tenfold radiant flux on the sample will increase the SNR by 10 dB for low  $N_O$  and low  $\alpha$ . For small values of  $\alpha$  the SNR increases until  $N_O = N/2$ , i.e. until reference and sample intensity are identical. For high values of  $\alpha$  the SNR decreases rapidly when going to a significant amount of sample photo electrons.

It is clearly seen that the SNR is only expected to increase linearly with  $\sqrt{N_O}$  for a small number of sample photons and a low value of  $\alpha$ . At higher numbers of sample photons the linear increase of coherence noise may even decrease the SNR when illumination of the sample is increased. Consequently, a filtering of coherence noise, as achieved by off-axis reference illumination and suitable filtering, should increase the SNR for high irradiation on the sample. Indeed, as shown in Table 2, the off-axis reference allows for an SNR gain of 8 dB being close to the theoretically expected maximum of 10 dB in the complete absence of coherence noise. The remaining 2 dB can be explained by incomplete filtering (remaining coherent noise due to filter selection), incoherent background noise being increased together with the sample illumination, or by decreased signal due to the higher lateral sampling frequency, where a lower modulation transfer of the camera is expected.

### 4.3 High imaging depth with off-axis holoscopy

In FF-SS-OCT optimal lateral resolution is limited to a region of the Rayleigh length around the focal plane. Due to the limited NA of the optical system of the eye, this does not exceed the thickness of the retina significantly. But imaging the anterior chamber or even the whole eye by a single shot measurement with good total resolution is still a challenge for OCT and needs ways to overcome the limited depth of focus.

Holoscopy applies refocusing techniques to the full-field OCT signals, restoring lateral resolution over tens of Rayleigh lengths. Combined with an off-axis reference wave maximal use of the coherence length of the swept laser source can be made, if reconstruction is only applied to the signal term. Fig. 7 shows a scattering sample of polyurethane resin doped with iron-oxide nanoparticles of sizes between 200 nm and 800 nm [24], where the signal term over positive and negative path lengths was successfully refocused. By using a numerical reconstruction technique for holoscopy [17, 18] backscattered light was detected with almost optimal lateral resolution in the full-range images over a depth of more than 10 mm.

Imaging the whole eye with FF-SS-OCT or holoscopy suffers from strong reflections at the different optical interfaces of the eye, which we expect to introduce significant autocorrelation noise or an increased noise floor when being incoherent with respect to the sample light. With off-axis recording and filtering of non-signal terms a complete *ex vivo* porcine eye, with both anterior and posterior segment, i.e. retina, lens, and cornea was imaged in a single data set (Fig. 8). The sweep range of the light source was reduced to 20 nm, sacrificing resolution for a total measurement depth of more than 25 mm when sampling the sweep with 2048 data points. By numerical refocusing on the signal term both retina and cornea were reconstructed sharply. To reduce noise, we acquired and averaged 9 volume data sets. Reflection induced artifacts and remaining DC signals were identified by their constant phase values in all images and removed numerically.

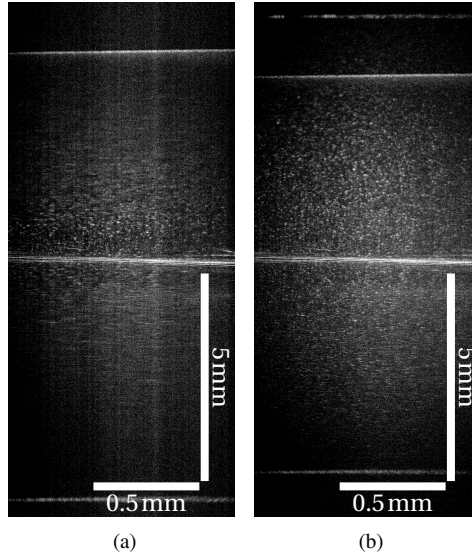


Figure 7: B-scan of nanoparticles randomly dispersed in polyurethane resin. Due to full-range recording the B-scan covers a depth of about 10mm. The central white structure marks the zero-delay line. At the imaging NA of 0.07 full lateral resolution was achieved only over a small axial depth of approximately two Rayleigh lengths  $2z_R \approx 100\mu\text{m}$  (a). When using digital refocusing techniques, the depth of focus was increased to nearly the full imaging depth (b).

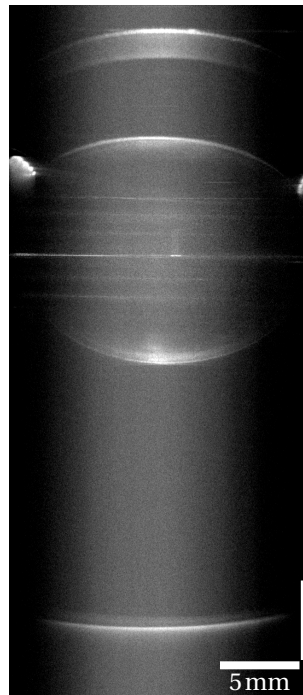


Figure 8: B-scan of an entire porcine eye including cornea, lens, and retina with an entire measurement depth of more than 25mm. During data acquisition the focus of the imaging optics was approximately on the retina. Later the image was numerically refocused to the iris. The focus on the retina could not be obtained as no lateral structures were visible to ensure correct focusing.

## 5 Conclusion and outlook

We demonstrated full-range imaging and suppression of autocorrelation artifacts by off-axis FF-SS-OCT and hologscopy. Dramatic improvement of image quality was shown for samples with highly reflecting layers such as a scotch tape roll. Furthermore, *in-vivo* images of the human retina show an increased SNR due to the reduction in coherence noise. Paral-

Parallelization of OCT imaging allows to increase the radiant flux which is directed into the eye without damaging the retina; the shown data was not yet limited by safety standards [25,26] and thus further increase in sensitivity is expected. Imaging speed of 39 MHz equivalent A-scan rate on-axis and 7 MHz off-axis were achieved, values which are two to three orders higher than today's clinical devices. These values are limited by the camera speed and the number of wavelengths sampled. By reducing resolution or imaging depth even higher values are possible. Since scanning does not limit the imaging speed multi-kHz volume rates are possible, which could measure fast retinal changes with submicrometer axial resolution. In the neuronal retina quality is comparable to scanned OCT system considering the high imaging speed. However, choroidal structures suffered from a strong background of multiply scattered light which could not be reduced by off-axis imaging. The presented *in-vivo* images show the potential of parallelized imaging of the neuronal retina, i.e., volumetric imaging at increased speed, resulting in full phase stability which is hardly achieved by the fastest spectrometer based OCT systems.

Holoscopy may also enable the imaging of the complete eye, i.e., anterior and posterior segment, with high resolution. The filtering of the image term in off-axis geometry doubles the imaging depth and suppresses spurious autocorrelation signals from ocular surfaces. A porcine eye was successfully imaged from cornea to retina using numerical refocusing of the signal term. However, the coherence length of the light source was not sufficient to acquire an entire human eye *in vivo*, yet.

Although off-axis imaging only uses parts of the lateral Fourier-space as oversampling is required to correctly capture the object wave field, using an additional angle for the reference wave that is different to the one used, a second signal could be acquired on the same camera. This way two independent wave fields could be multiplexed in a single image, which could for example be used for polarization sensitive measurements.

## Acknowledgments

This work was sponsored by the German Federal Ministry of Education and Research (Program "Innovative Imaging and Intervention", contract numbers 98729873C and 98729873E).

## References

- [1] B. Potsaid, I. Gorczynska, V. J. Srinivasan, Y. Chen, J. Jiang, A. Cable, and J. G. Fujimoto, "Ultrahigh speed spectral / fourierdomain oct ophthalmic imaging at 70,000 to 312,500 axial scans per second," *Opt. Express* **16**, 15149–15169 (2008).
- [2] B. Považay, A. Unterhuber, B. Hermann, H. Sattmann, H. Arthaber, and W. Drexler, "Full-field time-encoded frequency-domain optical coherence tomography," *Opt. Express* **14**, 7661–7669 (2006).
- [3] T. Bonin, G. Franke, M. Hagen-Eggert, P. Koch, and G. Hüttmann, "In vivo fourier-domain full-field oct of the human retina with 1.5 million a-lines/s," *Opt. Lett.* **35**, 3432–3434 (2010).
- [4] H. Spahr, D. Hillmann, C. Hain, C. Pfäffle, H. Sudkamp, G. Franke, and G. Hüttmann, "Imaging pulse wave propagation in human retinal vessels using full-field swept-source optical coherence tomography," *Opt. Lett.* **40**, 4771–4774 (2015).
- [5] D. Hillmann, H. Spahr, C. Hain, H. Sudkamp, G. Franke, C. Pfäffle, C. Winter, and G. Hüttmann, "Aberration-free volumetric high-speed imaging of in vivo retina," *Sci. Rep.* **6**, 35209 (2016).
- [6] D. Hillmann, H. Spahr, C. Pfäffle, H. Sudkamp, G. Franke, and G. Hüttmann, "In vivo optical imaging of physiological responses to photostimulation in human photoreceptors," *Proceedings of the National Academy of Sciences* **113**, 13138–13143 (2016).
- [7] I. Grulkowski, J. J. Liu, B. Potsaid, V. Jayaraman, C. D. Lu, J. Jiang, A. E. Cable, J. S. Duker, and J. G. Fujimoto, "Retinal, anterior segment and full eye imaging using ultrahigh speed swept source oct with vertical-cavity surface emitting lasers," *Biomed. Opt. Express* **3**, 2733–2751 (2012).
- [8] E. N. Leith and J. Upatnieks, "Reconstructed wavefronts and communication theory," *J. Opt. Soc. Am.* **52**, 1123–1128 (1962).
- [9] U. Schnars and W. P. O. Jüptner, "Digital recording and numerical reconstruction of holograms," *Meas. Sci. Technol.* **13**, R85 (2002).
- [10] U. Schnars and W. Jueptner, *Digital holography: digital hologram recording, numerical reconstruction, and related techniques* (Springer, 2005).



- [11] M. K. Kim, “Principles and techniques of digital holographic microscopy,” *SPIE Reviews* **1**, 018005 (2010).
- [12] D. Hillmann, G. Franke, L. Hinkel, T. Bonin, P. Koch, and G. Hüttmann, “Off-axis full-field swept-source optical coherence tomography using holographic refocusing,” (2013).
- [13] D. J. Fechtig, T. Schmoll, B. Grajciar, W. Drexler, and R. A. Leitgeb, “Line-field parallel swept source interferometric imaging at up to 1 MHz,” *Opt. Lett.* **39**, 5333–5336 (2014).
- [14] Y. Yasuno, S. Makita, T. Endo, G. Aoki, M. Itoh, and T. Yatagai, “Simultaneous b-m-mode scanning method for real-time full-range fourier domain optical coherence tomography,” *Appl. Opt.* **45**, 1861–1865 (2006).
- [15] D. L. Marks, T. S. Ralston, S. A. Boppart, and P. S. Carney, “Inverse scattering for frequency-scanned full-field optical coherence tomography,” *J. Opt. Soc. Am. A* **24**, 1034–1041 (2007).
- [16] B. J. Davis, D. L. Marks, T. S. Ralston, P. S. Carney, and S. A. Boppart, “Interferometric synthetic aperture microscopy: Computed imaging for scanned coherent microscopy,” *Sensors* **8**, 3903–3931 (2008).
- [17] D. Hillmann, C. Lühns, T. Bonin, P. Koch, and G. Hüttmann, “Holoscopy—holographic optical coherence tomography,” *Opt. Lett.* **36**, 2390–2392 (2011).
- [18] D. Hillmann, G. Franke, C. Lühns, P. Koch, and G. Hüttmann, “Efficient holoscopy image reconstruction,” *Opt. Express* **20**, 21247–21263 (2012).
- [19] G. L. Franke, D. Hillmann, T. Claußen, C. Lühns, P. Koch, and G. Hüttmann, “High resolution holoscopy,” *Proc. SPIE* **8213**, 821324 (2012).
- [20] D. Hillmann, C. Lühns, T. Bonin, P. Koch, A. Vogel, and G. Hüttmann, “Holoscopy: holographic optical coherence tomography,” *Proc. SPIE* **8091**, 80911H (2011).
- [21] N. Pavillon, C. S. Seelamantula, J. Kühn, M. Unser, and C. Depeursinge, “Suppression of the zero-order term in off-axis digital holography through nonlinear filtering,” *Appl. Opt.* **48**, H186–H195 (2009).
- [22] J. Goodman, *Speckle Phenomena in Optics: Theory and Applications* (Roberts & Company, 2007).
- [23] B. Baumann, S. O. Baumann, T. Konegger, M. Pircher, E. Götzinger, F. Schlanitz, C. Schütze, H. Sattmann, M. Litschauer, U. Schmidt-Erfurth, and C. K. Hitzenberger, “Polarization sensitive optical coherence tomography of melanin provides intrinsic contrast based on depolarization,” *Biomed. Opt. Express* **3**, 1670–1683 (2012).
- [24] P. D. Woolliams, R. A. Ferguson, C. Hart, A. Grimwood, and P. H. Tomlins, “Spatially deconvolved optical coherence tomography,” *Appl. Opt.* **49**, 2014–2021 (2010).
- [25] German Standard DIN EN 60825, *Sicherheit von Laser-Einrichtungen – Teil 1: Klassifizierung von Anlagen, Anforderungen und Benutzer-Richtlinien* (2008).
- [26] European Standard DIN EN ISO 15004-2, *Ophthalmic instruments – Fundamental requirements and test methods – Part 2: Light hazard protection* (2007).